

Forecasting the cross correlation of Terahertz Intensity Mapper [CII] line intensity maps with Euclid galaxies.

JUSTIN S. BRACKS ^{1,2,3} RYAN P. KEENAN ⁴ SHUBH AGRAWAL ³ GARRETT K. KEATING ⁵ JAMES E. AGUIRRE ³
ADAM LIDZ ³ CHARLES M. BRADFORD ^{6,2} BROCKTON BRENDALE ⁷ JEFFREY P. FILIPPINI ⁷ JIANYANG FU ⁸
KAROLINA GARCIA ⁹ CHRISTOPHER GROPPI ¹⁰ STEVE HAILEY-DUNSHEATH ² REINIER M.J. JANSSEN ^{6,2}
WOOSEOK KANG ¹¹ LUN-JUN LIU ² IAN LOWE ¹² ALEX MANDUCA ³ DANIEL P. MARRONE ¹²
PHILIP MAUSKOPF ¹³ EVAN C. MAYER ¹² SYDNEE O'DONNELL ⁷ TALIA SAEID ^{13,6} SIMON TARTAKOVSKY ⁸
MATHILDE VAN CUYCK ¹⁴ JOAQUIN VIEIRA ^{14,7,15} AND JESSICA A. ZEBROWSKI ^{11,16,17}

¹Department of Physics and Astronomy, University of California, Los Angeles, CA 90025, USA

²California Institute of Technology, 1200 E California Blvd, Pasadena, CA 91125, USA

³Department of Physics and Astronomy, University of Pennsylvania, Philadelphia, PA 19104, USA

⁴Max-Planck-Institut für Astronomie, Königstuhl 17, D-69117 Heidelberg, Germany

⁵Center for Astrophysics, Harvard & Smithsonian, Cambridge, MA, 02067, USA

⁶Jet Propulsion Laboratory, Caltech Institute of Technology, Pasadena, CA 91109, USA

⁷Department of Physics, Grainger College of Engineering, University of Illinois Urbana-Champaign, Urbana, IL 61801, USA

⁸Department of Physics, Princeton University, Princeton, NJ 08544, USA

⁹National Center for Supercomputing Applications, University of Illinois Urbana-Champaign, Urbana, IL 61801, USA

¹⁰Department of Physics and Applied Physics, University of Massachusetts, Lowell, Lowell, MA 01854, USA

¹¹Department of Astronomy and Astrophysics, University of Chicago, Chicago, IL 60637, USA

¹²Department of Astronomy, University of Arizona, Tucson, AZ 85721, USA

¹³School of Earth and Space Exploration, Arizona State University, Tempe, AZ 85287, USA

¹⁴Department of Astronomy, University of Illinois Urbana-Champaign, Urbana, IL 61801, USA

¹⁵Center for Astrophysical Surveys, National Center for Supercomputing Applications, University of Illinois Urbana-Champaign, Urbana, IL 61801, USA

¹⁶Fermi National Accelerator Laboratory, Batavia, IL, 60510, USA

¹⁷Kavli Institute for Cosmological Physics, University of Chicago, Chicago, IL, 60637, USA

ABSTRACT

We forecast that the Terahertz Intensity Mapper (TIM) cross-correlated with Euclid's Fornax deep field (EDF-F), TIM×EDF-F, will detect the [CII]-galaxy cross-power spectrum at a median redshift of 1.1 with $\gtrsim 7\sigma$ confidence. The Poisson component of the cross-power spectrum at $0.1 \leq k \leq 10$ hMpc⁻¹ (i.e. cross-shot noise) will be detected at $\gtrsim 3\sigma$ in 4 bins spanning $0.5 < z < 1.7$. This measurement will constrain the mean [CII] specific intensity over half of cosmic history and assess the degree to which Euclid-selected galaxies account for the [CII] intensity observed by TIM. We find that TIM can detect the cross-power spectrum across a wide range of [CII] intensity models.

1. INTRODUCTION

Understanding the history of cosmic star formation and its connection to galaxy evolution is one of the most important challenges in modern astrophysics. The nature of the galaxies responsible for the bulk of star formation has evolved over cosmic time (Casey et al. 2014). Half of the total energy output from the cosmic star formation has been absorbed by interstellar dust and re-emitted in the far-infrared (FIR) (Hauser & Dwek 2001; Lagache et al. 2005). Most star formation has occurred in dust-obscured environments (Madau & Dickinson 2014a; Zavala et al. 2021), and the most powerful starburst events in cosmic history are effectively invis-

ble at ultraviolet and optical wavelengths (Walter et al. 2012; Marrone et al. 2018). The path to understanding galaxy evolution thus necessarily runs through observations in the mid- and far-infrared, and requires reliable indicators of obscured star formation.

The energy output from cosmic star formation is partially reprocessed into dust continuum emission, but also into a variety of bright, unextincted FIR lines. These lines provide powerful diagnostics of star formation rates (SFR), supermassive black hole accretion rates, the spectrum of ionizing radiation, and the metallicity of the interstellar medium (ISM) (Hollenbach &

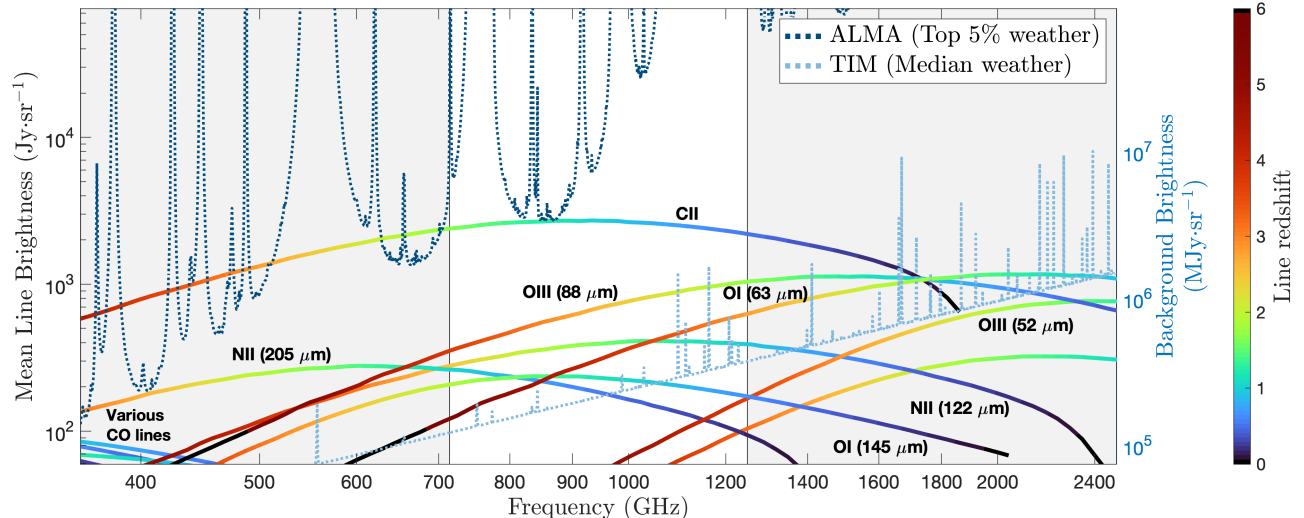


Figure 1. The specific intensity of select FIR line species (left y-axis) versus observed frequency. The dotted lines (using right y-axis) represent the thermal atmospheric background brightness at the ALMA site (dark) and at typical scientific ballooning altitudes (light). The color bar denotes the redshift corresponding to line emission at a given observed frequency. The white region shows TIM’s range of operation. Predicted line intensities for CO are based on models from Keating et al. (2020), calibrated on data from Kamenetzky et al. (2016). Line intensity predictions for [CII], [NII]₁₂₂, [NII]₂₀₅, [OI]₆₃, and [OIII]₅₂ are based on empirical models from the SimIM modeling framework (Keenan et al. 2020, 2022; Keating et al. 2020). Line intensity predictions for [OI]₁₄₅ and [OIII]₈₈ are based on models from Bonato et al. (2019). The atmospheric brightness is derived using the AM software package (Paine 2024).

Tielens 1997, 1999; Meixner et al. 2019; Schaan & White 2021a; Bernl & Kovetz 2022).

The [CII]-158 μm line is particularly important, as it is a primary coolant of the ISM (Draine 2011). [CII] is typically the brightest gas-phase feature emitted by galaxies, accounting for up to 1% of the total FIR luminosity (Draine 2011). This makes [CII] a promising observational tracer of cosmic star formation. Its brightness and ubiquity within haloes also make it a promising probe for mapping the large-scale structure of the universe (Fonseca et al. 2017; Moradinezhad Dizgah & Keating 2019; Karkare et al. 2022). Careful empirical work has gone into calibrating [CII] as a tracer of the star-formation rate (De Looze et al. 2014; Herrera-Camus et al. 2015), while the advent of ALMA has established the line as a powerful probe of ISM properties at redshifts beyond $z \geq 4$ (e.g., Le Fèvre et al. 2020; Spilker et al. 2022; Topping et al. 2022; Schaerer et al. 2020). Studies of [CII] emission are helping to reveal dust-obscured star formation at these high redshifts (Loiacono et al. 2021; Grupioni et al. 2020) and are likely necessary to complement the rest-frame UV view of high-redshift star formation provided by JWST (Williams et al. 2023; Harikane et al. 2023; Schouws et al. 2025).

However, the Earth’s atmosphere is partially opaque and emissive at mid- to far-infrared wavelengths, making observations of [CII] and other FIR lines at $z \lesssim 4$ very difficult from ground-based facilities. Many FIR obser-

vations are only possible from stratospheric or space-based platforms. Figure 1 presents the relative line brightnesses for several key emission lines, and contrasts the atmospheric brightness at the ALMA site (considering only the best 5% of weather days) with that at a scientific balloon’s float altitude ($\sim 36\text{km}$). Here we see that [CII] is the dominant emission line across most of the FIR regime ($< 2\text{ THz}$). At wavelengths that target the redshifted [CII] line at $z \sim 1$, a ground-based telescope contends with at least an order of magnitude greater background brightness than a stratospheric platform.

Additionally, connecting the physical processes observed in individual galaxies to large-scale structure will require wide-field mapping in the spatial and spectral dimensions. Surveys of molecular and atomic lines have been typically limited to small fields of view and subject to significant sampling uncertainty at cosmological redshifts (Keenan et al. 2020).

Line Intensity Mapping (LIM) is an emerging approach for capturing the 3D structure of the universe via large-scale, volumetric measurements (for a review see Chang & Lidz 2026). The LIM technique measures the amplitude of intensity fluctuations as a function of spatial scale, capturing the statistical characteristics of the emitting sources. Keating et al. (2016); Keating et al. (2020) report initial shot regime detections of CO signal ($k \gtrsim 1 h\text{ Mpc}^{-1}$). There have also been detections using

Full System			
Temperature	250mK		
Diameter	2.0 m		
Illumination	cryogenic Lyot stop restricts to ~ 1.9 m diameter		
Survey Area	$1^\circ \times 1^\circ$		
Detector Yield	85%		
Total Transmission	8%		
Resolving Power	$R \approx 250$		
Spectrometer	Short Wavelength	Long Wavelength	
Detector Array Format	51×64	51×64	spatial \times spectral
Wavelength range	240 – 317	317 – 420	μ m
$\Delta\nu$	4.3	3.3	GHz
Beam FWHM	37	48	arcsec
NEI (median)	124.5	64.2	10^7 Jy/sr \sqrt{s}
[CII] redshift range	0.52–1.0	1.0–1.67	
[CII] cosmic epoch	5.9–8.5	3.9–5.9	Gyr of cosmic age

Table 1. Design characteristics for TIM. The upper table lists characteristics of the full system or that are shared by both detector modules. The lower table reports properties of the spectrometer for the short and long wavelength modules.

the hydrogen 21 cm line in cross-correlation with traditional galaxy surveys (Chang et al. 2010; Amiri et al. 2023; Cunnington et al. 2023; Masui et al. 2013; Switzer et al. 2013).

It is currently challenging for LIM surveys to achieve robust auto-power spectrum measurements, especially since the field is relatively young. A range of systematic challenges need to be overcome (Bernal & Kovetz 2022). For instance, the IR continuum is expected to be at least 2 orders of magnitude brighter than [CII] line emission. Additionally, foreground emitters and line interlopers further confuse potential detections.

Fortunately, LIM lends itself very well to cross-correlation between pairs of surveys that cover overlapping redshift ranges with different tracers. This can serve as a means of alleviating or circumventing some of the most insidious challenges. Cross-correlation avoids an average bias from unshared foregrounds and line-interlopers, where emission from a source other than the target line is redshifted into the target spectral band.

Cross-correlations of line intensity maps with the matter density field, as traced by spectroscopic galaxy surveys (LIM-Gal), will be a particularly potent approach for line intensity mappers targeting low and modest redshift ranges ($z \lesssim 2$) where galaxy surveys can measure relatively large proportions of the galaxy population. The signal-to-noise ratio (SNR) of LIM-Gal measurements is driven, in part, by the number density, $n_{\text{Gal}}(z)$ of galaxies in the galaxy survey at the requisite redshifts. Due to their intrinsic flux limits, contemporary galaxy surveys suffer a decline in $n_{\text{Gal}}(z)$ beyond $z \approx 1$ (Momcheva et al. 2016). Cross-correlation with

a LIM survey across this drop-off in sensitivity can inform how much of the galaxy luminosity function is being missed as a function of redshift. In this regime, an infrared LIM survey in cross-correlation with a spectroscopic galaxy survey yields considerable discovery potential, while also providing robust cross-checks from a tried-and-true method. Further, the comparably high SNR that galaxy surveys bring to the table significantly boosts the SNR in the cross-power spectrum relative to the line’s auto spectrum. This approach has already served as a critical proof of concept in 21 cm cosmology (Pen et al. 2009; Chang et al. 2010; Masui et al. 2013; Anderson et al. 2018; Wolz et al. 2022; Cunnington et al. 2023; Switzer et al. 2013) and been explored for a range of early submillimeter and FIR LIM measurements (Pullen et al. 2013; Pullen et al. 2018; Yang et al. 2019; Keenan et al. 2022).

In this paper, we emphasize the capabilities of the forthcoming Terahertz Intensity Mapper (TIM), a NASA-funded project to carry out a [CII] LIM survey from a stratospheric balloon, specifically in cross-correlation with the *Euclid* space telescope’s deep field, Fornax.

The paper is organized as follows. Section 2 presents the as-built, or as-designed characteristics and limitations of the TIM. Section 3 describes the forecasting formalism for the cross-correlation measurement between a [CII] LIM experiment and a spectroscopic galaxy survey. Then, we detail any assumptions or approximations that we adopt in our fiducial forecast. Section 4 presents the salient outcomes of our investigation, and reports the implications of our cross-correlation forecasts for con-

straining the [CII] history. We conclude in section 5, and briefly discuss a potential successor experiment to TIM. Finally, we include an appendix, A where we motivate our decision to use EDF-F as our primary cross-correlator over comparable surveys.

In the following, we assume the Planck 2018 cosmological parameters (Aghanim et al. 2020). In all calculations requiring a star formation rate density (SFRD), we assume Kroupa initial mass functions, converting between IMFs using table 1 from Kennicutt & Evans (2012) where necessary.

2. TIM

A number of [CII] line intensity mapping instruments will become operational in the coming years (e.g TIME, CCAT, EXCLAIM) (Vieira et al. 2020; Crites 2022; Choi & Collaboration 2023; Essinger-Hileman et al. 2020), and numerous second-generation instruments exploiting advances in submillimeter/terahertz instrumentation are also under consideration. At the same time, densely sampled, wide field spectroscopic surveys using space-based grism spectroscopy are now greatly expanding the footprints of galaxy surveys suitable for cross-correlation measurements (Mellier et al. 2024; Pozzetti et al. 2016; Mowla et al. 2022; Momcheva et al. 2016). Here we overview one such LIM instrument suitable for [CII] LIM at $z \sim 1$ – TIM.

The upcoming Terahertz Intensity Mapper experiment (Vieira et al. 2020; Marrone et al. 2022) is a balloon-borne far infrared telescope to be flown from Antarctica in the austral summer of 2027-2028. TIM is designed to map [CII] at the peak and drop off of cosmic star formation, $0.52 < z < 1.67$ ($240\mu\text{m} \leq \lambda \leq 420\mu\text{m}$). As shown in figure 1, [CII] is the brightest FIR line in the wavelength range we target, reducing contamination from interloper lines. [CII] is robust against dust extinction. These qualities make [CII] an ideal diagnostic line for characterizing the history and nature of otherwise dust-obscured star forming galaxies (Lagache 2017; Gruppioni et al. 2020). As shown in figure 1, the atmosphere is largely opaque to terahertz photons. TIM must make its observations from above the majority of the atmosphere, driving the need for a balloon platform.

TIM uses cryogenically cooled kinetic inductance detectors (KIDs). KIDs are a promising approach to large-format far-IR detector arrays in which each detector pixel is a lithographically patterned superconducting microresonator (Zmuidzinas 2012 for a review). TIM will employ two optically separated detector modules, the short wavelength array (SWA) ($240\mu\text{m} - 317\mu\text{m}$), and the long wavelength array (LWA) ($317\text{ microns} - 420\text{ microns}$). A module is comprised of four subarrays each

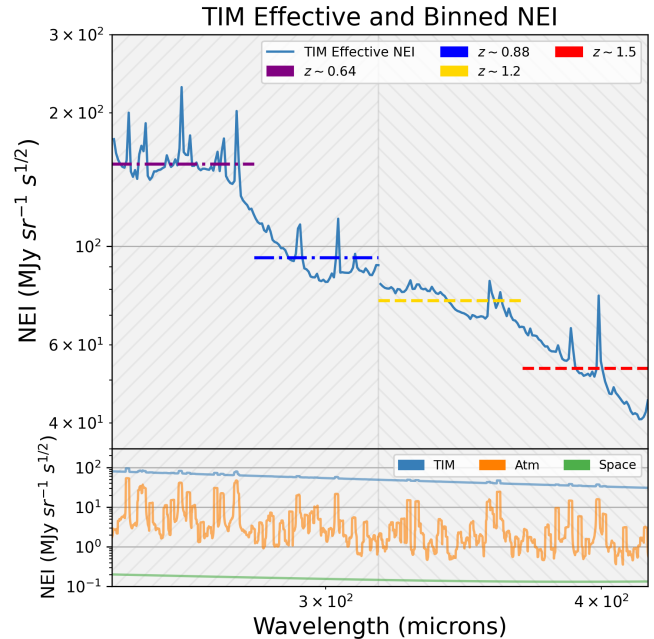


Figure 2. **Top** Nominal NEI for the TIM detector focal planes. We present the averaged NEI for TIM’s 4 redshift bins separately in purple, blue, yellow and red, depicting increasing redshift. Gray-filled areas denote the wavelength bands for TIM’s SWA (upward hashed) and LWA (downward hashed). TIM’s band-averaged NEI is shown by dashed (SWA) and dash-dotted (LWA) horizontal lines. The NEI for the current TIM instrument is dominated by the Poisson noise imparted by the warm primary mirror. **Bottom** We include equivalent curves for both a stratospheric atmosphere (orange) and zodiacal-background-light (green) limited version of the TIM optics.

housing roughly 1,000 KIDs. The bandwidths of SWA and LWA are represented in Figure 2 by the upward and downward grey hashed regions, respectively. In the following forecasts we further split the TIM redshift range at the centers of both the SWA and LWA modules to create four TIM redshift bins centered at approximately $z = 0.64, 0.9, 1.2, 1.5$. The average total noise equivalent intensity (NEI) seen by the TIM detectors in each of these redshift bins is shown in figure 2. The TIM KIDs noise characteristics are subdominant to the contribution from the experiment’s ambient-temperature primary mirror, which is the primary source of system noise. For comparison, we have included the NEI profiles for an atmosphere-limited version of TIM, as well as a background-limited (zodiacal light primarily) version that could be achieved by a space mission.

3. CROSS-SPECTRUM FORMALISM

In a cross-spectrum, we consider the correlation between the intensity fields of two tracers. In this section, we review a formalism for cross-correlating two inde-

pendent tracer phenomena. We begin by adopting the cross-correlation formalism put forth in [Schaan & White \(2021b\)](#) for the correlation of two line emission intensity fields. We then specify this formalism toward the cross-correlation between one emission line and the galaxy overdensity field.

3.1. The Line-Line Formalism

Following [Schaan & White \(2021b\)](#), the redshift- and scale-dependent cross-power spectrum of two surveys can be expressed as the summed contributions from the 2-halo, 1-halo, and shot-power terms, which respectively capture the contributions from the large-scale distribution of matter, the distribution of galaxies within their dark matter halos, and a Poisson term due to the discrete locations of individual emitters:

$$P_{i \times j}(k, z) = P_1^{\text{Halo}}(k, z) + P_2^{\text{Halo}}(k, z) + P_{\text{shot}}^\times(z) \quad (1)$$

The two-halo term can be defined as:

$$P_2^{\text{Halo}} = b_i(z)b_j(z)\langle I_i(z)\rangle\langle I_j(z)\rangle P_M(k, z) \quad (2)$$

b_i and b_j are the linear biases of tracers i and j relative to the matter over-density field with power spectrum P_M . The average specific intensity of emission i at redshift z , $\langle I_i(z)\rangle$ is given by

$$\langle I_i\rangle = \frac{c}{4\pi H(z)\nu_i} \int \phi(L_i)L_i dL_i \quad (3)$$

where ϕ is the luminosity function of line i .

The 1-halo term can be expressed as:

$$P_1^{\text{Halo}} = \frac{U_\times^2(k)}{n_{h,\times}} \langle I_i(z)\rangle\langle I_j(z)\rangle \quad (4)$$

where U_\times and $n_{h,\times}$ describe the tracer weighted profile and number density of dark matter halos. P_1^{Halo} is a second-order term with considerable complexity from a modeling standpoint. We omit this term from our fiducial forecast, which modestly suppresses the forecast power at intermediate scales ($k \approx 1 \text{ hMpc}^{-1}$) in comparison to similarly motivated models which include the 1-halo term (perhaps most conveniently illustrated by comparing the ‘‘Keenan+22’’ and ‘‘This Work’’ lines in figure 5).

Finally, the cross-shot power spectrum can be calculated as

$$P_{\text{shot}}^\times = \left(\frac{c}{4\pi H(z)}\right)^2 \frac{1}{\nu_i\nu_j} \int \int dL_i dL_j \Phi(L_i, L_j)L_i L_j \quad (5)$$

Where Φ is the joint distribution function describing the number of galaxies per unit volume of luminosities L_i and L_j in the two tracer lines.

3.2. Modeling the [CII] \times Galaxy Overdensity Field Cross-Power Spectrum

The cross-correlation between a line intensity map and a galaxy survey can be thought of as a special case of the line-line cross-power spectrum (Eq 1), where $I_{\text{Gal}}(z)$ is taken to be $1 + \delta_{\text{Gal}}$ and δ_{Gal} is the overdensity field of the galaxies in the survey. By construction, the ‘mean intensity’ is unity and unitless; $\langle I_{\text{Gal}}\rangle = 1$. The cross-shot noise component arises from the Fourier transform of the self-correlation term, i.e. contributions to $\langle I_i(\mathbf{x}_1)\delta_{\text{Gal}}(\mathbf{x}_2)\rangle$ at a single point, $\mathbf{x}_1 = \mathbf{x}_2$. This reflects the contribution of galaxies in the traditional survey to the specific intensity in the LIM observations. In Fourier space this gives

$$P_{\text{shot}}^\times = f_s \langle I_i\rangle / n_{\text{Gal}} \quad (6)$$

where $n_{\text{Gal}}(z)$ is the number density of galaxies in the galaxy catalog and f_s is the fraction of $\langle I_i\rangle$ that can be attributed to galaxies in the galaxy catalog.

To obtain a plausible model value for f_s , we compare the SFRD in the ASTRODEEP catalogue as presented in [Merlin et al. \(2021\)](#) to the SFRD curve in [Madau & Dickinson \(2014a\)](#), resulting in $f_s \sim 0.9$.

Because both the ASTRODEEP catalog and the EDF-F catalog have similar limiting magnitude and spectral resolution (see table 2), we can approximate their f_s values as equal.

Here we are implicitly assuming that $L_{[\text{CII}]} \propto \text{SFR}$ for all systems (similar to [Yang et al. \(2022\)](#) and related models). In this case, the fraction of the total [CII] intensity produced by the galaxies matches the fraction of the SFRD they produce - modulo scatter in the $L_{[\text{CII}]} - \text{SFR}$ relation. The effect of this scatter is averaged down in a large sample and is negligible.

Continuing with the assumption that $\langle I_{[\text{CII}]} \rangle$ closely traces star formation, we parameterize the integral in equation 3 as

$$\int dL_{[\text{CII}]} \phi(L_{[\text{CII}]})L_{[\text{CII}]} = L_0 \dot{\rho}_*(z) \quad (7)$$

Here $\dot{\rho}_*$ is the SFRD, and L_0 is the line emission luminosity from a galaxy with a star formation rate of $1M_\odot/\text{yr}$ - in other words, the line luminosity per unit SFR. $\dot{\rho}_*(z)$ is assumed to follow the parameterized history from [Madau & Dickinson \(2014b\)](#). To determine $L_0^{[\text{CII}]}$, we assume a simple ratio-metric power law relationship between the average [CII] luminosity and the overall IR luminosity, choosing to employ the full galaxy population value presented in Table 3 of [De Looze et al. \(2014\)](#) (slope of 1.01).

The matter power spectrum, $P_M(k, z)$ is approximated by the linear theory prediction, which should

be adequate on the spatial scales where the clustering signal dominates over the cross-shot noise contribution $k \lesssim 1 h \text{Mpc}^{-1}$. We compute $P_M(k, z)$ using *CAMB* (Lewis & Challinor 2011).

To develop a quantitative estimate of the bias values for the galaxy and [CII] surveys considered in this investigation, we solve the auto-power spectrum ($P_{i \times i} \equiv P_{[CII]}$) of equation 1 for the b_i parameter in the two-halo term (see eq. 2). We then obtain $P_{[CII]}$ and $\langle I_{[CII]}(z) \rangle$ using SimIM (Keenan et al. 2020). From this we attain $b_{[CII]}$. For the central redshift of each of TIM’s four redshift bins; this yields $b_{[CII]}(z \approx 0.65, 0.89, 1.18, 1.5) \approx 1.22, 1.35, 1.6, 1.87$, which agrees with the b_{Gal} values determined by Durkalec et al. (2015) (under the assumption that linear galaxy bias traces star formation) and Jullo et al. (2012). Since we are now assuming that both $b_{[CII]}$ and b_{Gal} closely trace the SFR, as an approximation in our model we set $b_{\text{Gal}} = b_{[CII]}$. In practice, b_{Gal} can be determined using the galaxy auto-power spectrum as well. Figure 3 shows our calculated value for $b_{[CII]}(z)$ and compared with the analogous $b_{[CII]}(z)$ values found by applying the same treatment to other $I_{[CII]}(z)$ models in the literature. We see that our values agree well with other models who derive their $I_{[CII]}(z)$ history from a [CII] - SFR relation such as Yang et al. (2022).

Neglecting the 1-halo term as discussed above, and applying equations 2 and 6 specifically to a [CII] LIM

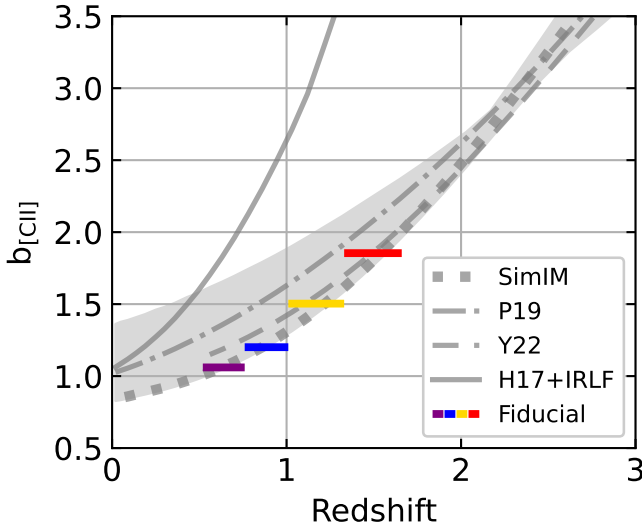


Figure 3. Redshift-dependent linear clustering bias models using separate model classes. The colored bars are the fiducial biases from this work, with the individual colors bearing the same meaning as in figure 2. Grey fill region display forecasts using similar models, effectively serving as a literature-based uncertainty on our assumed biases. Dot-dashed gray line: Padmanabhan (2019), dashed gray line: Yang et al. (2022), dotted gray line: Keenan et al. (2020).

survey in cross-correlation with a spectroscopic galaxy survey as discussed in the introduction, Equation 1 becomes

$$P_{[CII] \times \text{Gal}} \equiv P_{\times} = b_{[CII]} b_{\text{Gal}} \langle I_{[CII]} \rangle P_M + f_s \langle I_{[CII]} \rangle / n_{\text{Gal}} \quad (8)$$

with z and k dependencies suppressed for clarity.

3.3. Cross spectral variance

Following Villaescusa-Navarro et al. (2015), the variance attributed to a LIM-Gal cross-power spectrum measurement can be written as:

$$\text{Var}[P_{\times}] = \frac{1}{2N_{\text{mode}}} \left[P_{\times}^2 + P_{\text{Gal}} \left(P_{[CII]} + \frac{P_N}{\mathcal{B}} \right) \right] \quad (9)$$

where \mathcal{B} is the instrument beam effect imposed on the [CII] signal. The beam term is discussed in the following sub-section, while the other terms (and special considerations) contributing to the cross-variance are discussed in the following bullets:

- P_{\times} , P_{Gal} , and $P_{[CII]}$ (the power spectral terms) account for sample variance in the clustering regime of the cross-power, galaxy auto power, and [CII] auto power, respectively, and in most cases (certainly true for TIM) are subdominant to the system noise terms. We have suppressed the scale and redshift dependence of P_{\times} , $P_{[CII]}$, and P_{Gal} for readability. The auto power spectra, $P_{[CII]}$ and P_{Gal} can be expressed using Eq 1, except we consider cross correlating each survey with itself such that $P_{[CII]} = b_{[CII]}^2 I_{[CII]}^2 P_M + P_{\text{shot}}^{[CII]}$ and $P_{\text{Gal}} = b_{\text{Gal}}^2 P_M + P_{\text{shot}}^{\text{Gal}}$. We compute $P_{\text{shot}}^{[CII]}$ using a semi-empirical model for the star formation rate distribution function (Behroozi et al. 2019) and convert this to a [CII] luminosity function using the SimIM modeling framework (Keenan et al. in prep), while $P_{\text{shot}}^{\text{Gal}} = 1/n_{\text{Gal}}$.
- P_N , the instrument noise power contribution from the [CII] survey can be expressed as $P_N = \sigma_P^2 V_{\text{vox}}$. Where V_{vox} is the comoving volume of an instrument voxel defined by the beam size (sky-transverse direction) and spectral resolution (line-of-sight direction). Here σ_P is the contribution from instrumental noise, which is proportional to the overall noise equivalent intensity (NEI) of the experiment in that band. For a survey that reaches a uniform depth across the whole map, σ_P can be approximated as:

$$\sigma_P \approx \text{NEI} \sqrt{\frac{N_{\text{pix}}}{N_{\text{det}} t S}} \quad (10)$$

Here t_S is the total integration time of the survey (assumed to be ~ 200 hrs for TIM), N_{pix} is the number of (2D) elements into which the map is pixelized, N_{det} is the number of detectors observing the same spectral range (see table 1), or spatially independent spectra observed simultaneously by the instrument.

- N_{mode} refers to the number of times an individual mode uniquely occurs in the spherically averaged volume captured by a survey. We discuss some nuances our approach imposes on the number of measurable samples per mode in the following two subsections.

3.3.1. Beam and Spectral Attenuation

An experiment's finite spectral and spatial resolutions impose limitations on the minimum measurable spatial extent in the line-of-sight and transverse directions, respectively. The wave-numbers corresponding to the physical scales represented by the spectral and spatial resolution elements can be calculated as $\sigma_{\parallel}(z) = L_{\parallel}(z)/\sqrt{8 \ln(2)}$ and $\sigma_{\perp}(z) = L_{\perp}(z)/\sqrt{8 \ln(2)}$, where L_{\parallel} is the comoving distance spanned by the detector spectral resolution (full width at half maximum [FWHM]), $d\nu$ at a redshift z , and L_{\perp} is the comoving distance spanned by the telescope beam FWHM at a specific redshift. As the measured scale approaches the resolution limit, the fidelity of the measurement suffers. The observed intensity fluctuations are attenuated by the finite angular and spectral resolutions of the instrument. We approximate the beam response as a Gaussian, which disperses the sky intensity in the perpendicular direction according to:

$$b(x, y) = \frac{1}{2\pi\sigma_{\perp}^2} \exp\left[-\frac{1}{2} \frac{x^2 + y^2}{\sigma_{\perp}^2}\right], \quad (11)$$

For simplicity, we also assume a Gaussian spectral response;

$$b(z) = \frac{1}{\sqrt{2\pi\sigma_{\parallel}^2}} \exp\left[-\frac{1}{2} \frac{z^2}{\sigma_{\parallel}^2}\right]. \quad (12)$$

We can combine the spatial and spectral resolution contributions into a three-dimensional attenuation function $B(x, y, z) = b(x, y)b(z)$. The Fourier transform $\mathcal{F}[B(x, y, z)]$ gives a wave number dependent transfer function describing the finite resolution effects, $\overline{B}(k_x, k_y, k_z)$:

$$\overline{B}(\mathbf{k}) = \exp\left[-\frac{1}{2}(k_x^2 + k_y^2)\sigma_{\perp}^2 - \frac{1}{2}k_z^2\sigma_{\parallel}^2\right] \quad (13)$$

where k_x , k_y and k_z are components of an individual mode, \mathbf{k} . Similarly, the survey geometry and spectral

bandwidth drive the maximum measurable spatial extents, which define the total survey *volume*, and therefore the minimum k modes. We take the conservative approach of removing any mode which has $k_i \approx 0$. That is, we do not count a mode if any of its directional components is 0. This has the effect of depressing N_{mode} where $k < 0.1 h \text{ Mpc}^{-1}$.

In the case of LIM-Gal where the positional accuracy of the galaxy survey far outstrips the LIM survey, we can treat the galaxy survey's x and y attenuation contributions as delta functions. That is, the only contribution to the attenuation function coming from the galaxy survey stems from the survey's spectral uncertainty.

For our analysis, we define a linear average of \overline{B} coefficients with a bin of width $d \ln(k)$:

$$\mathcal{B} = \frac{1}{N_k} \sum_{k-\delta k}^{k+\delta k} \overline{B} \quad (14)$$

3.3.2. Survey Area and N_{mode}

In general, there is a practical trade-off between sky coverage and survey depth. Increasing the survey area augments the number of samples per mode. This could decrease variance without the need to make any hardware changes. However, increasing survey area further divides the survey time, resulting in less integration time per voxel and leading to a corresponding increase in P_N .

In the case of the auto-power, the optimal survey area is simply chosen such that $P_N \approx P_{\text{[CI]}}(k)$. A larger area will inflict a considerable noise penalty. However, this is not necessarily the case in the cross-spectrum. For our purposes, we discuss this in the context of a [CII] \times Galaxy Survey cross-spectrum, but the following is generally true for LIM cross-spectra: In the limit that the LIM measurement variance is dominated by instrumental noise, i.e. $P_N \gg P_{\text{[CI]}}$ and $P_N P_{\text{Gal}} \gg P_{\times}^2$, Eq 9 becomes:

$$\text{Var}[P_{\times}] = \frac{1}{2N_{\text{mode}}} \left(\frac{P_N}{\mathcal{B}} P_{\text{gal}} \right) \quad (15)$$

Because both N_{mode} and P_N scale linearly with the survey area, this limit yields the surprising result that (for a particular k mode) there is no optimal survey area. That is, for the cross-spectrum, as the survey area grows, the map noise increases owing to the decreasing observing time per voxel, but this is exactly compensated by the gain in the number of modes sampled. Note that this supposes the galaxy survey spans the entire enlarged [CII] survey area at adequate depth. It also assumes that the modes of interest are well-sampled, i.e., their wavelengths are small compared to the survey dimensions and captured given the angular/spectral resolution of the [CII] experiment.

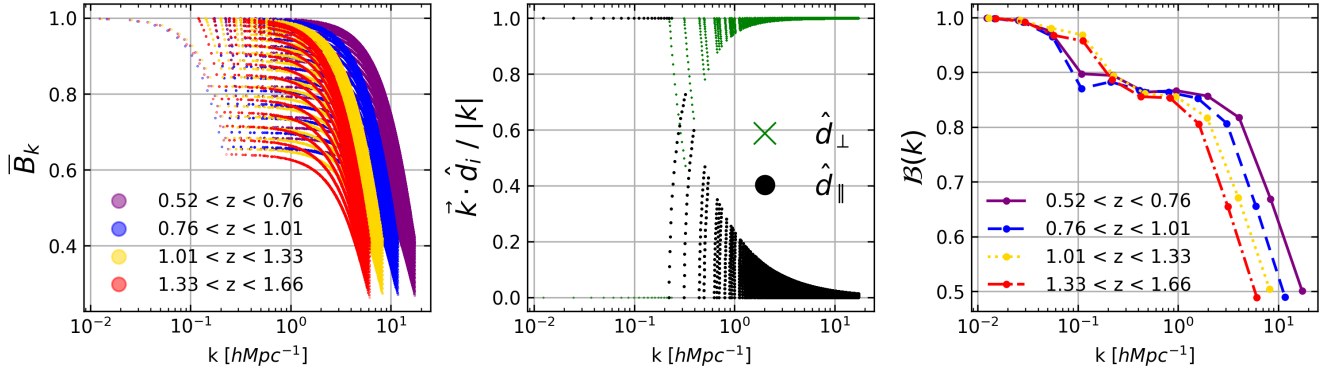


Figure 4. *left:* $\bar{B}(k)$, the transfer coefficient for each individual k mode measured by TIM in each of its 4 redshift bins. *center:* Projection of each mode \mathbf{k} in the transverse (k_{\perp}) and line-of-sight (k_{\parallel}) directions for TIM’s lowest redshift ($0.52 < z < 0.77$) bin. *right:* The linear average of $\bar{B}(k)$ within logarithmically spaced, spherical shells in k -space denoted $B(k)$.

3.4. Retrieving $\langle I_{[\text{CII}]} \rangle$ and $SFRD(z)$

By isolating and dividing out $\langle I_{[\text{CII}]} \rangle$ from equation 8 we obtain:

$$\langle I_{[\text{CII}]} \rangle = \frac{P_{\times}}{b_{[\text{CII}]} b_{\text{Gal}} P_M + f_s / n_{\text{Gal}}}. \quad (16)$$

If the terms in the denominator are known, an estimate of $I_{[\text{CII}]}(z)$ can then be derived from the inverse-variance-weighted average over all k . Given the modest SNR of TIM, P_M and b_{Gal} can be treated as known constants derived from the standard cosmological model and the galaxy survey respectively. The remaining terms, $b_{[\text{CII}]}$ and f_s must be approximated, and contribute an additional systematic uncertainty to the derivation of $I_{[\text{CII}]}(z)$. The range of empirical models in Figure 3 (gray filled region) suggests this uncertainty is around $\pm 20\%$ for $b_{[\text{CII}]}$. Because the *Euclid* deep fields (as TIM’s primary cross-correlator) will probe significantly below the knee of the $\text{H}\alpha$ luminosity function, we expect the galaxy catalog to account for the majority of the cosmic star formation rate density and $I_{[\text{CII}]}(z)$. This suggests $f_s \gg 50\%$, with correspondingly small uncertainties. Estimates of f_s will improve once the depth and completeness of the *Euclid* deep fields is better characterized (Le Brun et al. 2025).

4. RESULTS

In this section we explore spectral and spatial resolution attenuation effects specific to TIM, discuss TIM’s ability to sample spatial scales with respect to $N_{\text{mode}}(k)$ and finally present TIM’s ability to constrain models of $\langle I_{[\text{CII}]} \rangle$ and the cosmic star formation history.

The three panels in figure 4 show the scale-dependent behavior of the beam window function (as formally introduced in Section 3.3.1) in the four TIM redshift bins. In the **leftmost panel** we present the \bar{B} coefficients for each unique mode sampled by the baseline TIM ex-

periment in cross-correlation with projected *Euclid* capabilities. Here we see that the bulk of the available k mode samples are concentrated toward higher k , or smaller scales. Then, as the physical scales approach the comoving distance subtended by the telescope beam, information is lost and \bar{B} falls off steeply.

The center panel of figure 4 shows the projection of each mode vector onto the line-of-sight direction. For clarity, this is only shown for TIM’s lowest redshift bin ($0.52 < z < 0.77$) but the other redshift bins behave similarly. This is shown to illustrate that modes below $k \sim 0.2 h\text{Mpc}^{-1}$ are *only* captured in the line-of-sight (k_{\parallel}) direction. This is due to the fact that TIM’s line-of-sight extent represents a much larger comoving scale than the largest scales probed in the transverse directions. Similarly, the physical scales subtended by the spectral resolutions of both TIM’s long- and short-wavelength modules translate to considerably greater physical extents than TIM’s spatial resolution, again meaning that each of TIM’s voxels are much longer in the spectral/line-of-sight direction than they are tall or wide in the spatial/transverse directions.

As we approach higher k ’s the contribution from the transverse (k_{\perp}) component increases, dominating by $k \sim 1 h\text{Mpc}^{-1}$. This transition from line-of-sight to transverse dominated regimes is reflected in the double-hump profile in **the rightmost panel** of figure 4. Here the average beam attenuation coefficient of samples in logarithmically spaced k bins tracks the few line-of-sight modes at low k , then transitions to tracking the lower coefficient, but much more densely sampled transverse-direction-dominated modes at high k . This affects the scale-dependent sensitivity of the TIM [CII] survey.

4.1. Sensitivity Forecast for the TIM [CII] Survey in Cross-Correlation with EDF-F

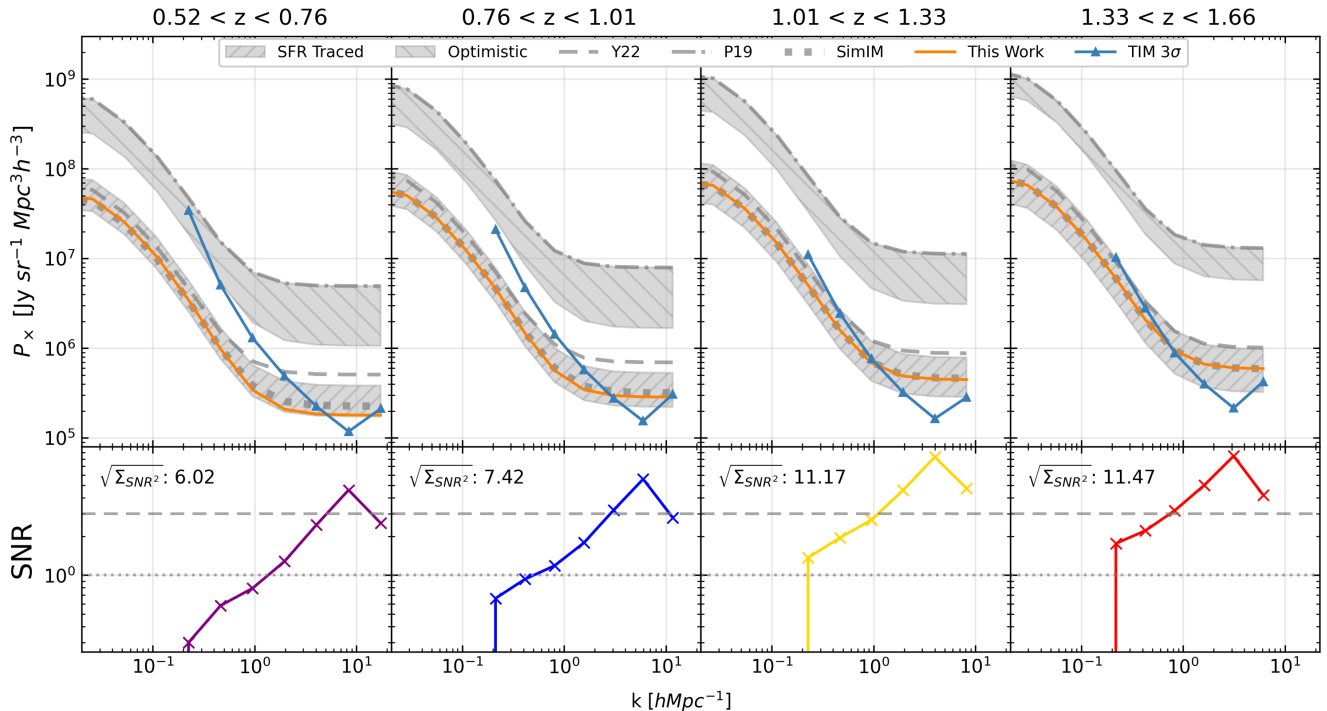


Figure 5. **Top:** Forecast TIM $P_{[CII] \times EDF-F}$ sensitivity curves in 4 redshift bins. Upward-facing arrows represent the 1σ sensitivity; blue solid line represents TIM as designed with a 1 deg^2 field; orange solid line the $P_{[CII] \times EDF-F}$ forecast from this work. Grey fill regions display analogous forecasts using parameters from alternative models in the current literature. Dot-dashed gray line: Padmanabhan (2019), Dashed gray line: Yang et al. (2022), dotted grey line: Keenan et al. (2020). **Bottom:** SNR per k bin, with total expected per-redshift-bin SNR presented in the upper left of each SNR subfigure. Dotted and dashed grey lines present 1σ and 3σ thresholds respectively.

We apply Eq 8 to determine TIM $[CII] \times EDF-F$ cross-power spectrum models for each TIM redshift bin. Dividing the power (Eq 8) by the square root of the variance (Eq 9) yields an SNR as a function of k in bins of $d \ln(k) = 1$, as shown in the lower panels of Figure 5. In the upper panels, we present TIM’s 3σ detection threshold as well as our model for the TIM $\times EDF-F$ intrinsic signal.

We forecast that TIM will secure robust detections of the shot power-dominated regime ($k > 1 \text{ h Mpc}^{-1}$) in all four redshift bins in cross-correlation with the EDF-F galaxy distribution, with only slightly higher SNR in the two higher redshift spectral bins with respect to the shot regime. In TIM’s two higher redshift bins, we predict successful detections of the transition from the $[CII]$ signal in the clustering regime ($k < 1 \text{ h Mpc}^{-1}$) to the shot regime. With decreasing $|k|$, the SNR suffers from two separate effects. First, the number of available mode samples decreases with k . Additionally, a higher proportion of available modes contain some directional component $k_i = 0$, and are therefore removed from our count. By $k \sim 0.1 \text{ h Mpc}^{-1}$, virtually no modes remain. If taken in aggregate (summed in quadrature), each of

TIM’s redshift bins should return a detection at a total SNR of at least 6.

The TIM SNR predictions presented in figure 5 are from our semi-analytical halo formalism-based model, shown by the solid orange lines in figure 5. Our forecast agrees well with the most conservative representatives of the model space, which assume that $I_{[CII]}(z)$ closely traces SFR. Here again, we forecast that TIM $\times Euclid$ will generate definitive detections of the cross-shot power in the four highest k bins extending across all redshift bins. In the two higher redshift bins, we expect to detect a roughly 1σ signal across all probable scales, extending to many σ detections in the case of the more optimistic model space.

In Figure 6 we report the inverse variance weighted average of $I_{[CII]}(z)$. This is done individually for each of TIM’s 4 redshift bins. Here we assume that the galaxy and $[CII]$ clustering bias factors follow the models in section 3.2. The upward arrows in Figure 6 present the 3σ sensitivity threshold toward the $I_{[CII]}(z)$ signal. Here we predict that TIM will fully constrain the $I_{[CII]}(z)$ history across $0.5 \lesssim z \lesssim 1.7$. These measurements will provide an independent view of the total (obscured and unobscured) star formation rate density of the universe

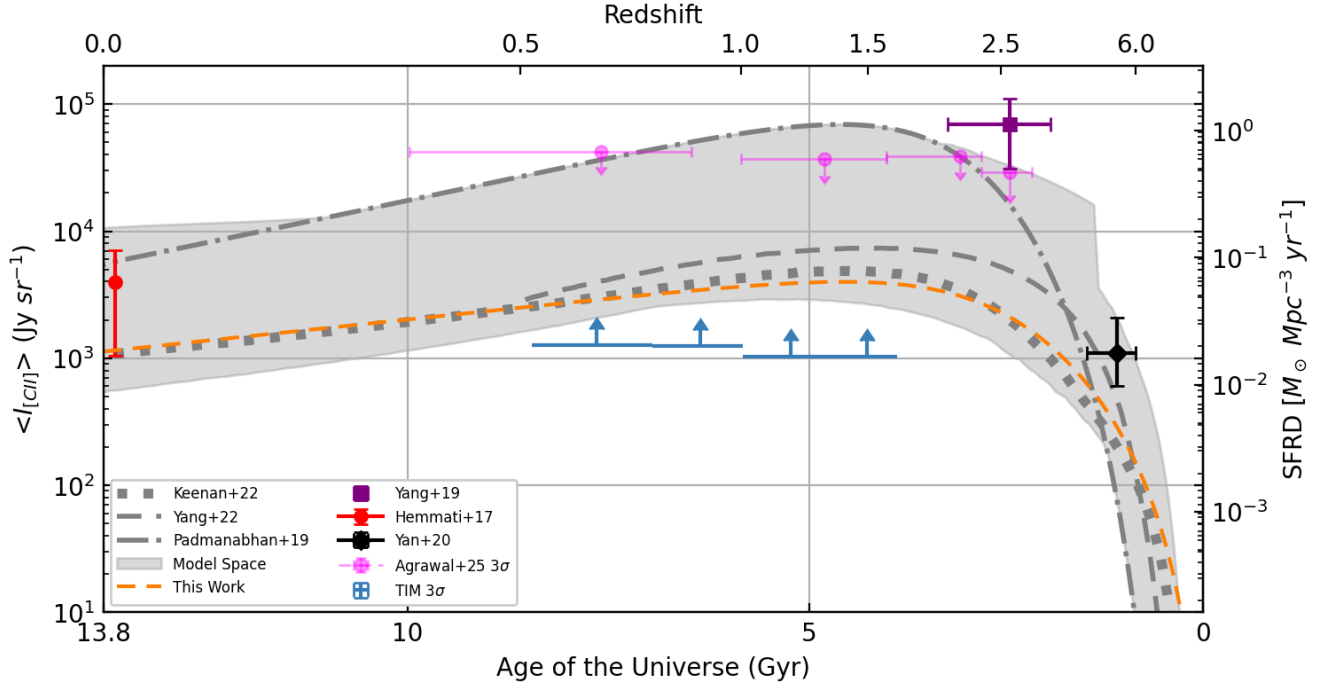


Figure 6. Forecast constraints on the mean specific intensity (left y axis) history of [CII], and correspondingly, the cosmic SFRD (right y axis) as a function of cosmic age (lower x axis) or redshift (upper x axis). The colored horizontal bars with upward-facing triangles represent the 3σ detection threshold forecasts for each of TIM’s 4 redshift bins. The pink bars with downward-facing arrows represent the 3σ upper limit found in (Agrawal et al. 2025); the bar widths represent the temporal widths of the corresponding redshift bins, we include nominal detections from Agrawal et al. (2025) (3σ upper limit), Hemmati et al. (2017) (1σ), Yang et al. (2019) (95% confidence), and Yan et al. (2020) (1σ) in pink, red, purple and black respectively. Grey fill regions display the $I_{\text{[CII]}}$ history model space represented in current literature. We include three representative models: Dot-dashed gray line from Padmanabhan (2019), Dashed gray line from Yang et al. (2022), dotted grey line from Keenan et al. (2020). The dashed orange line shows the average [CII] intensity/SFRD forecast in this work.

over a large fraction of cosmic time. In the grey-filled region we include the model space spanned by some commonly considered literature. (The discontinuity at $z \sim 1$ is due to the fact that one model does not extend to $z = 0$.)

4.2. Discussion

Achieving robust auto-power detections at higher redshift and building a deep and precise inventory of the SFRD history will require the implementation of surveys that are capable of both the depth and breadth of field to overcome cosmic variance uncertainties. This will require wider fields of view, which in turn require either increased detector hours or decreased atmospheric/instrumental loading of FIR detectors - ideally, both. In figure 7, we compare the detection power of the TIM experiment as built, against a next-generation TIM-like experiment which simply replaces TIM’s warm 2m mirror with a cold 0.5m mirror (see fig 2 for the corresponding atmosphere-limited NEI curve), and assumes a 4 deg^2 survey field; we hold all other experimental parameters constant, including the 200 hour survey

time. By integrating a cold-mirror approach similar to the design of the *PIPER* and *EXCLAIM* (Gandilo et al. 2016; Cataldo et al. 2020) balloon payloads, an \sim order of magnitude increase in sensitivity could be achieved. A complementary paper, Agrawal et al. (in prep.), further explores the prospect of galaxy cross-correlation with hypothetical successors to TIM (i.e., balloon and space far-infrared spectrometers). Agrawal et al. (in prep.) also forecasts the sensitivity of TIM in cross-correlation with other LIM tracers, which provide complementary information to the galaxy cross-correlation in both the clustering and shot regimes.

5. CONCLUSION

[CII] LIM-based constraints on the SFRD history are highly complementary to existing measurements. [CII] can provide an unbiased accounting of dust-obscured star formation, avoiding the dust corrections required of UV-based measurements. At the same time, intensity mapping constrains the faint end of the luminosity function, probing galaxies too faint to be directly detected in IR continuum surveys. Because the LIM-Gal

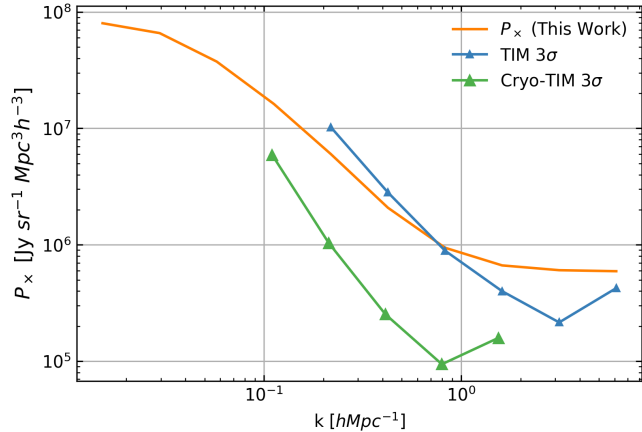


Figure 7. 3σ galaxy-cross-power-spectrum detection thresholds for TIM (blue) and a nominal next-generation TIM-like experiment, Cryo-TIM (green) in TIM’s $1.33 < z < 1.66$ band. Assuming a 4 deg^2 field and an atmosphere-limited, 4 Kelvin, 0.5m primary mirror for Cryo-TIM, and holding all other parameters constant between experiments.

cross-shot power is sensitive to the coincident presence of star formation in both the LIM and galaxy surveys, the shot regime measurement will be particularly helpful in informing the level to which our galaxy catalogs undercount low mass and dust-obscured galaxies as a function of redshift.

Additionally, the wide-field nature of LIM – especially with future mission concepts – also gives rise to field sizes much larger than typical extra-galactic deep fields, providing a robust check on the field-to-field variance that is often a challenge for surveys with narrow field instruments like HST, JWST, and ALMA.

We have reviewed a simple formalism for computing the expected signal strength and error in a cross-power spectrum between a line intensity map and the overdensity field of a spectroscopic galaxy survey. We explored the expected SNR on this cross-correlation for the case of the imminent TIM [CII] survey, taken with the upcoming Euclid Deep Field Fornax. We forecast that this approach will produce definitive constraints on the star formation history. TIM will confirm or rule out speculative models of the $I_{[\text{CII}]}(z)$ history, and will, at the very least, provide robust detections of the cross-power spectral shot signal during cosmic noon.

With the ability to push to deeper redshifts, near-future balloon experiments will be able to fill the $1 < z < 3$ gap where [CII] must be studied from above the atmosphere. At greater redshifts, facilities like FYST equipped with instruments like EoR-Spec will be able to probe [CII] out to the epoch of reionization. This will give us a wide-field, unbiased view of the cosmic SFR history, using a single, well-calibrated tracer, essentially

covering from reionization to cosmic noon. This would enable cross-correlations of the [CII] signal with nearly any other emission line across the vast majority of the universe’s history, allowing astronomers to probe relative chemical abundances as well as the contributions of certain line species toward the aggregate emission of small, low-metallicity galaxies (Schaan & White 2021a).

Finally, TIM serves as a pathfinder mission with respect to both data analysis techniques and hardware development for upcoming missions. For instance, this study, and TIM’s science goals, are deeply relevant and complementary to PRIMA (Probe far-Infrared Mission for Astrophysics), a NASA Astrophysics Probe Explorer concept for a 1.8 m, ≈ 4.5 K cryogenic far-infrared ($\approx 24\text{--}261 \mu\text{m}$) observatory (Glenn et al. 2025). Similarly, as this first generation of LIM experiments come online, they enable not only a wealth of data, also a wealth of possibility for near-term growth in astrophysics and cosmology.

ACKNOWLEDGMENTS

Work on the Terahertz Intensity Mapper is supported by the National Aeronautics and Space Administration under grants 80NSSC19K1242 and 80NSSC24K1881 issued through the Science Mission Directorate.

S.A. and J.A. note that this publication was made possible through the support of Grant 63040 from the John Templeton Foundation. The opinions expressed in this publication are those of the authors and do not necessarily reflect the views of the John Templeton Foundation. S.A.’s work was also supported by the Quad Fellowship.

Part of this research was carried out at the Jet Propulsion Laboratory, California Institute of Technology, under a contract with the National Aeronautics and Space Administration (80NM0018D0004).

	$R_{\text{spec}} (\lambda/\Delta\lambda)$	$L_{\text{lim}} (\text{Mag})$	$A_{\text{Surv}} (\text{deg}^2)$	A_{over}	z_{over}	Filter/Spectrometer
EDF-F	450	~ 24	10	100%	100%	Red & Blue Grisms / H α
astroDEEP	350-450	~ 24	0.08	40%	100%	Various NIR
Roman	461	~ 24	2000	100%	$\sim 50\%$	G150 / H α
3D-DaSh	350	24.74	1.35	0%	100%	F160W

Table 2. Parameters of four example galaxy surveys with which the TIM lineage of telescopes could cross-correlate. L_{lim} is the luminosity of a point source that would yield a 5σ detection. A_{over} and z_{over} reference the survey’s field and redshift overlaps with TIM respectively. Filters and Spectrometers are referred to by the monikers set down in the literature (no attempt was made to standardize naming convention across experiments).

APPENDIX

A. SURVEYS AND EXPERIMENTS

Cross-correlations with optical and infrared galaxy catalogues offer high SNR cross-checks on LIM. In the limit that P_{Gal} is dominated by its shot-noise term ($1/n_{\text{Gal}}$), the SNR of a LIM-Gal power spectrum is heavily dependent on the galaxy catalogue’s number density. Therefore, the utility of a galaxy survey for LIM cross-correlations depends on the minimum detectable luminosity, L_{min} , of the galaxies in the traditional survey. A relatively low limiting luminosity is required to achieve a sufficiently high n_{gal} and thus mitigate shot-noise contributions to the cross-power spectrum variance. This is currently challenging at high redshifts, e.g. $z \gtrsim 2$, do to a lack of sufficiently deep galaxy surveys, but fairly routine at the redshifts of interest for TIM, $0.5 \lesssim z \lesssim 1.7$.

Table 2 serves as a quick reference and summary of the following discussion of some galaxy surveys which are potential cross-correlators for the TIM experiment (and future TIM-like experiments). Certain HST legacy catalogues offer sufficient n_{Gal} for cross-correlations, but suffer from sky coverage limitations. The 3D-DASH catalogue (Mowla et al. 2022) is a ~ 1.43 square degree survey of the equatorial COSMOS field, which entirely encompasses TIM’s redshift range, and fully covers TIM’s target field size. 3D-DASH probed galaxies with luminosities down to $\sim 25^{\text{th}}$ magnitude ($M_{AB} \approx 24.7$) for point sources. This catalogue *would* be ideal for cross-correlations with the baseline, first-generation TIM experiment. As an Antarctic balloon experiment, TIM is unable to view COSMOS and other more northerly fields. A subsequent long-duration balloon flight at a higher latitude could make great use of both the 3D-DASH catalogue and the increase in the technological readiness level of necessary flight and detector hardware made by the TIM collaboration.

Similarly, the ASTRODEEP-GS34 (Merlin et al. 2021) catalogue is an existing compilation of spectroscopic and photometric detections of galaxies in the GOOD-S field. ASTRODEEP / CANDELS is one of the deepest and densest catalogues of spectroscopic galaxies currently available. However, the relatively small field of GOODS-S and the ASTRODEEP catalogue ($\approx 0.08\text{deg}^2$) imposes a steep limitation on its potential science yield in cross-correlation with LIM surveys, which typically aim to map regions of $> 0.1\text{deg}^2$ to avoid uncertainty from sample variance. ASTRODEEP provides a promising proof of concept. A similar, but wider galaxy catalogue would yield even more valuable science data.

Ground-based, wide-field, spectrographic galaxy surveys have achieved impressive breadth in terms of survey area. Still, they generally lack the number density necessary for successful cross-correlations in $\sim \text{deg}^2$ fields such as those targeted by TIM. Fortunately, upcoming and ongoing space telescopes will provide deep and wide-field spectroscopic galaxy catalogues. For instance, NASA’s Nancy Grace Roman Space Telescope, *Roman*, is forecast to detect redshifted H α line emitting galaxies from $1 \lesssim z \lesssim 2$ in numbers comparable to the CANDELS catalog across vastly larger regions of the sky. This will overlap in redshift with TIM’s long wavelength module only (Wang et al. 2022; Pozzetti et al. 2016). More relevant for TIM’s purposes, given it’s timeline and observing capabilities, is the recently launched *Euclid* space telescope which will map the galaxy distribution at high sensitivity using the redshifted H α line (Mellier et al. 2024). *Euclid*’s deep-field Fornax (EDF-F) is a $\sim 10\text{deg}^2$ field positioned over Chandra deep-field south (100 times the field area over ASTRODEEP). This calibration field promises the most complete galaxy population for cross-correlation with the TIM [CII] survey. While the *Euclid* wide survey will employ only their red grism, EDF-F is being probed with both the experiment’s red and blue grisms (Jahnke et al. 2024). Their combined wavelength sensitivity

traces the H α line at $0.42 \lesssim z \lesssim 1.8$. *Euclid* will probe this field down to an absolute magnitude of $\gtrsim 24$ in both its wavelength bands. This will match the galaxy number density of ASTRODEEP at $z \sim 1$ and more than double the ASTRODEEP n_{Gal} by $z = 2$ (Pozzetti et al. 2016). We will adopt EDF-F as our galaxy catalogue cross-correlator for the remainder of this work.

REFERENCES

- Aghanim, N., Akrami, Y., Ashdown, M., et al. 2020, *A&A*, 641, A6, doi: [10.1051/0004-6361/201833910](https://doi.org/10.1051/0004-6361/201833910)
- Agrawal, S., Aguirre, J., & Keenan, R. 2025, *Astronomy & Astrophysics*, doi: [10.1051/0004-6361/202556503](https://doi.org/10.1051/0004-6361/202556503)
- Agrawal, S., Aguirre, J., Keenan, R., et al. in prep.
- Amiri, M., Bandura, K., Chen, T., et al. 2023, *ApJ*, 947, 16, doi: [10.3847/1538-4357/acb13f](https://doi.org/10.3847/1538-4357/acb13f)
- Anderson, C., Luciw, N., Li, Y.-C., et al. 2018, *Monthly Notices of the Royal Astronomical Society*, 476, 3382
- Behroozi, P., Wechsler, R. H., Hearin, A. P., & Conroy, C. 2019, *MNRAS*, 488, 3143, doi: [10.1093/mnras/stz1182](https://doi.org/10.1093/mnras/stz1182)
- Bernal, J. L., & Kovetz, E. D. 2022, *The Astronomy and Astrophysics Review*, 30, 5
- Bonato, M., De Zotti, G., Leisawitz, D., et al. 2019, *PASA*, 36, e017, doi: [10.1017/pasa.2019.8](https://doi.org/10.1017/pasa.2019.8)
- Casey, C. M., Narayanan, D., & Cooray, A. 2014, *PhR*, 541, 45, doi: [10.1016/j.physrep.2014.02.009](https://doi.org/10.1016/j.physrep.2014.02.009)
- Cataldo, G., Ade, P. A., Anderson, C. J., et al. 2020, in *Ground-based and Airborne Telescopes VIII*, Vol. 11445, SPIE, 469–479
- Chang, T.-C., & Lidz, A. 2026, *Line-Intensity Mapping*. <https://arxiv.org/abs/2602.03011>
- Chang, T.-C., Pen, U.-L., Bandura, K., & Peterson, J. B. 2010, *Nature*, 466, 463
- Choi, S., & Collaboration, C.-p. 2023, *Bulletin of the AAS*, 55
- Crites, A. T. 2022, in *Millimeter, Submillimeter, and Far-Infrared Detectors and Instrumentation for Astronomy XI*, ed. J. Zmuidzinas & J.-R. Gao, Vol. PC12190, International Society for Optics and Photonics (SPIE), PC121900I, doi: [10.1117/12.2630647](https://doi.org/10.1117/12.2630647)
- Cunnington, S., Li, Y., Santos, M. G., et al. 2023, *MNRAS*, 518, 6262, doi: [10.1093/mnras/stac3060](https://doi.org/10.1093/mnras/stac3060)
- Cunnington, S., Li, Y., Santos, M. G., et al. 2023, *Monthly Notices of the Royal Astronomical Society*, 518, 6262
- De Looze, I., Cormier, D., Lebouteiller, V., et al. 2014, *A&A*, 568, A62, doi: [10.1051/0004-6361/201322489](https://doi.org/10.1051/0004-6361/201322489)
- De Looze, I., Cormier, D., Lebouteiller, V., et al. 2014, *A&A*, 568, A62, doi: [10.1051/0004-6361/201322489](https://doi.org/10.1051/0004-6361/201322489)
- Draine, B. T. 2011, *Physics of the Interstellar and Intergalactic Medium*
- Durkalec, A., Le Fèvre, O., Pollo, A., et al. 2015, *A&A*, 583, A128, doi: [10.1051/0004-6361/201425343](https://doi.org/10.1051/0004-6361/201425343)
- Essinger-Hileman, T. M., Oxholm, T. M., Siebert, G. L., et al. 2020, in *Millimeter, Submillimeter, and Far-Infrared Detectors and Instrumentation for Astronomy X*, ed. J. Zmuidzinas & J.-R. Gao (SPIE), doi: [10.1117/12.2576254](https://doi.org/10.1117/12.2576254)
- Fonseca, J., Silva, M. B., Santos, M. G., & Cooray, A. 2017, *MNRAS*, 464, 1948, doi: [10.1093/mnras/stw2470](https://doi.org/10.1093/mnras/stw2470)
- Gandilo, N. N., Ade, P. A., Benford, D., et al. 2016, in *Millimeter, Submillimeter, and Far-Infrared Detectors and Instrumentation for Astronomy VIII*, Vol. 9914, SPIE, 372–379
- Glenn, J., Meixner, M., Bradford, C. M., et al. 2025, *Journal of Astronomical Telescopes, Instruments, and Systems*, 11, 031628, doi: [10.1117/1.JATIS.11.3.031628](https://doi.org/10.1117/1.JATIS.11.3.031628)
- Gruppioni, C., Béthermin, M., Loiacono, F., et al. 2020, *A&A*, 643, A8, doi: [10.1051/0004-6361/202038487](https://doi.org/10.1051/0004-6361/202038487)
- Gruppioni, C., Béthermin, M., Loiacono, F., et al. 2020, *Astronomy & Astrophysics*, 643, A8
- Harikane, Y., Ouchi, M., Oguri, M., et al. 2023, *ApJS*, 265, 5, doi: [10.3847/1538-4365/acaaa9](https://doi.org/10.3847/1538-4365/acaaa9)
- Hauser, M. G., & Dwek, E. 2001, *ARA&A*, 39, 249, doi: [10.1146/annurev.astro.39.1.249](https://doi.org/10.1146/annurev.astro.39.1.249)
- Hemmati, S., Yan, L., Diaz-Santos, T., et al. 2017, *The Astrophysical Journal*, 834, 36, doi: [10.3847/1538-4357/834/1/36](https://doi.org/10.3847/1538-4357/834/1/36)
- Herrera-Camus, R., Bolatto, A. D., Wolfire, M. G., et al. 2015, *ApJ*, 800, 1, doi: [10.1088/0004-637X/800/1/1](https://doi.org/10.1088/0004-637X/800/1/1)
- Hollenbach, D. J., & Tielens, A. G. G. M. 1997, *ARA&A*, 35, 179, doi: [10.1146/annurev.astro.35.1.179](https://doi.org/10.1146/annurev.astro.35.1.179)
- . 1999, *Reviews of Modern Physics*, 71, 173, doi: [10.1103/RevModPhys.71.173](https://doi.org/10.1103/RevModPhys.71.173)
- Jahnke, K., Gillard, W., Schirmer, M., et al. 2024, *Euclid. III. The NISP Instrument*. <https://arxiv.org/abs/2405.13493>
- Jullo, E., Rhodes, J., Kiessling, A., et al. 2012, *The Astrophysical Journal*, 750, 37, doi: [10.1088/0004-637X/750/1/37](https://doi.org/10.1088/0004-637X/750/1/37)
- Kamenetzky, J., Rangwala, N., Glenn, J., Maloney, P. R., & Conley, A. 2016, *ApJ*, 829, 93, doi: [10.3847/0004-637X/829/2/93](https://doi.org/10.3847/0004-637X/829/2/93)
- Karkare, K. S., Moradinezhad Dizgah, A., Keating, G. K., Breyse, P., & Chung, D. T. 2022, *arXiv e-prints*, arXiv:2203.07258, doi: [10.48550/arXiv.2203.07258](https://doi.org/10.48550/arXiv.2203.07258)
- Keating, G. K., Marrone, D. P., Bower, G. C., & Keenan, R. P. 2020, *The Astrophysical Journal*, 901, 141, doi: [10.3847/1538-4357/abb08e](https://doi.org/10.3847/1538-4357/abb08e)
- Keating, G. K., Marrone, D. P., Bower, G. C., et al. 2016, *ApJ*, 830, 34, doi: [10.3847/0004-637X/830/1/34](https://doi.org/10.3847/0004-637X/830/1/34)
- Keenan, R. P., Keating, G. K., & Marrone, D. P. 2022, *The Astrophysical Journal*, 927, 161
- Keenan, R. P., Marrone, D. P., & Keating, G. K. 2020, *The Astrophysical Journal*, 904, 127

- Kennicutt, R. C., & Evans, N. J. 2012, *Annual Review of Astronomy and Astrophysics*, 50, 531–608, doi: [10.1146/annurev-astro-081811-125610](https://doi.org/10.1146/annurev-astro-081811-125610)
- Lagache, G. 2017, *Proceedings of the International Astronomical Union*, 12, 228
- Lagache, G., Puget, J.-L., & Dole, H. 2005, *ARA&A*, 43, 727, doi: [10.1146/annurev.astro.43.072103.150606](https://doi.org/10.1146/annurev.astro.43.072103.150606)
- Le Brun, V., Bethermin, M., Moresco, M., et al. 2025, Euclid Quick Data Release (Q1) – Characteristics and limitations of the spectroscopic measurements. <https://arxiv.org/abs/2503.15308>
- Le Fèvre, O., Béthermin, M., Faisst, A., et al. 2020, *A&A*, 643, A1, doi: [10.1051/0004-6361/201936965](https://doi.org/10.1051/0004-6361/201936965)
- Lewis, A., & Challinor, A. 2011, CAMB: Code for Anisotropies in the Microwave Background, *Astrophysics Source Code Library*, record ascl:1102.026
- Loiacono, F., Decarli, R., Gruppioni, C., et al. 2021, *A&A*, 646, A76, doi: [10.1051/0004-6361/202038607](https://doi.org/10.1051/0004-6361/202038607)
- Madau, P., & Dickinson, M. 2014a, *ARA&A*, 52, 415, doi: [10.1146/annurev-astro-081811-125615](https://doi.org/10.1146/annurev-astro-081811-125615)
- . 2014b, *ARA&A*, 52, 415, doi: [10.1146/annurev-astro-081811-125615](https://doi.org/10.1146/annurev-astro-081811-125615)
- Marrone, D. P., Spilker, J. S., Hayward, C. C., et al. 2018, *Nature*, 553, 51, doi: [10.1038/nature24629](https://doi.org/10.1038/nature24629)
- Marrone, D. P., Aguirre, J. E., Bracks, J. S., et al. 2022, in *Millimeter, Submillimeter, and Far-Infrared Detectors and Instrumentation for Astronomy XI*, Vol. 12190, SPIE, 131–142
- Masui, K., Switzer, E., Banavar, N., et al. 2013, *The Astrophysical Journal Letters*, 763, L20
- Meixner, M., Cooray, A., Leisawitz, D., et al. 2019, arXiv e-prints, arXiv:1912.06213, doi: [10.48550/arXiv.1912.06213](https://doi.org/10.48550/arXiv.1912.06213)
- Mellier, Y., Abdurro'uf, Barroso, J. A. A., et al. 2024, Euclid. I. Overview of the Euclid mission. <https://arxiv.org/abs/2405.13491>
- Merlin, E., Castellano, M., Santini, P., et al. 2021, *A&A*, 649, A22, doi: [10.1051/0004-6361/202140310](https://doi.org/10.1051/0004-6361/202140310)
- Momcheva, I. G., Brammer, G. B., Van Dokkum, P. G., et al. 2016, *The Astrophysical Journal Supplement Series*, 225, 27
- Moradinezhad Dizgah, A., & Keating, G. K. 2019, *ApJ*, 872, 126, doi: [10.3847/1538-4357/aafd36](https://doi.org/10.3847/1538-4357/aafd36)
- Mowla, L. A., Cutler, S. E., Brammer, G. B., et al. 2022, *ApJ*, 933, 129, doi: [10.3847/1538-4357/ac71af](https://doi.org/10.3847/1538-4357/ac71af)
- Padmanabhan, H. 2019, *MNRAS*, 488, 3014, doi: [10.1093/mnras/stz1878](https://doi.org/10.1093/mnras/stz1878)
- Paine, S. 2024, The am atmospheric model, 14.0, Zenodo, doi: [10.5281/zenodo.13748391](https://doi.org/10.5281/zenodo.13748391)
- Pen, U.-L., Staveley-Smith, L., Peterson, J. B., & Chang, T.-C. 2009, *Monthly Notices of the Royal Astronomical Society: Letters*, 394, L6
- Pozzetti, L., Hirata, C. M., Geach, J. E., et al. 2016, *A&A*, 590, A3, doi: [10.1051/0004-6361/201527081](https://doi.org/10.1051/0004-6361/201527081)
- Pullen, A. R., Chang, T.-C., Doré, O., & Lidz, A. 2013, *The Astrophysical Journal*, 768, 15, doi: [10.1088/0004-637X/768/1/15](https://doi.org/10.1088/0004-637X/768/1/15)
- Pullen, A. R., Serra, P., Chang, T.-C., Doré, O., & Ho, S. 2018, *MNRAS*, 478, 1911, doi: [10.1093/mnras/sty1243](https://doi.org/10.1093/mnras/sty1243)
- Schaan, E., & White, M. 2021a, *Journal of Cosmology and Astroparticle Physics*, 2021, 067
- . 2021b, *Journal of Cosmology and Astroparticle Physics*, 2021, 068, doi: [10.1088/1475-7516/2021/05/068](https://doi.org/10.1088/1475-7516/2021/05/068)
- Schaerer, D., Ginolfi, M., Béthermin, M., et al. 2020, *A&A*, 643, A3, doi: [10.1051/0004-6361/202037617](https://doi.org/10.1051/0004-6361/202037617)
- Schouws, S., Bouwens, R. J., Algera, H., et al. 2025, Deep Constraints on [CII]158 μ m in JADES-GS-z14-0: Further Evidence for a Galaxy with Low Gas Content at $z=14.2$. <https://arxiv.org/abs/2502.01610>
- Spilker, J. S., Hayward, C. C., Marrone, D. P., et al. 2022, *ApJL*, 929, L3, doi: [10.3847/2041-8213/ac61e6](https://doi.org/10.3847/2041-8213/ac61e6)
- Switzer, E. R., Masui, K. W., Bandura, K., et al. 2013, *Monthly Notices of the Royal Astronomical Society: Letters*, 434, L46, doi: [10.1093/mnrasl/slt074](https://doi.org/10.1093/mnrasl/slt074)
- Topping, M. W., Stark, D. P., Endsley, R., et al. 2022, *Monthly Notices of the Royal Astronomical Society*, 516, 975–991, doi: [10.1093/mnras/stac2291](https://doi.org/10.1093/mnras/stac2291)
- Vieira, J., Aguirre, J., Bradford, C. M., et al. 2020, arXiv preprint arXiv:2009.14340
- Villaescusa-Navarro, F., Viel, M., Alonso, D., et al. 2015, *Journal of Cosmology and Astroparticle Physics*, 2015, 034, doi: [10.1088/1475-7516/2015/03/034](https://doi.org/10.1088/1475-7516/2015/03/034)
- Walter, F., Decarli, R., Carilli, C., et al. 2012, *Nature*, 486, 233, doi: [10.1038/nature11073](https://doi.org/10.1038/nature11073)
- Wang, Y., Zhai, Z., Alavi, A., et al. 2022, *The Astrophysical Journal*, 928, 1
- Williams, C. C., Alberts, S., Ji, Z., et al. 2023, arXiv e-prints, arXiv:2311.07483, doi: [10.48550/arXiv.2311.07483](https://doi.org/10.48550/arXiv.2311.07483)
- Wolz, L., Pourtsidou, A., Masui, K. W., et al. 2022, *Monthly Notices of the Royal Astronomical Society*, 510, 3495
- Yan, L., Sajina, A., Loiacono, F., et al. 2020, *The Astrophysical Journal*, 905, 147, doi: [10.3847/1538-4357/abc41c](https://doi.org/10.3847/1538-4357/abc41c)
- Yang, S., Popping, G., Somerville, R. S., et al. 2022, *ApJ*, 929, 140, doi: [10.3847/1538-4357/ac5d57](https://doi.org/10.3847/1538-4357/ac5d57)

Yang, S., Pullen, A. R., & Switzer, E. R. 2019, Monthly Notices of the Royal Astronomical Society: Letters, 489, L53–L57, doi: [10.1093/mnrasl/slz126](https://doi.org/10.1093/mnrasl/slz126)

Zavala, J. A., Casey, C. M., Manning, S. M., et al. 2021, ApJ, 909, 165, doi: [10.3847/1538-4357/abdb27](https://doi.org/10.3847/1538-4357/abdb27)
Zmuidzinas, J. 2012, Annual Review of Condensed Matter Physics, 3, 169, doi: [10.1146/annurev-conmatphys-020911-125022](https://doi.org/10.1146/annurev-conmatphys-020911-125022)